

Deposition of a Metal–Organic Heterostructure to Form Magnetic–Nonmagnetic Bilayer Films

Sudipta Pal,[†] Neena Susan John,[‡] P. John Thomas,[‡] G. U. Kulkarni,[‡] and Milan K. Sanyal^{*,†}

Surface Physics Division, Saha Institute of Nuclear Physics, 1/AF Bidhannagar, Kolkata 700 064, India, and Chemistry and Physics of Materials Unit, Jawaharlal Nehru Center for Advanced Scientific Research, Jakkur, Bangalore 560064, India

Received: October 7, 2003; In Final Form: May 11, 2004

Langmuir–Blodgett deposition of a nonmagnetic–magnetic metal–organic bilayer film is reported here. The bilayers consist of a Au nanocluster upper layer over a monolayer of gadolinium stearate (GdSt) deposited on a hydrophilic Si(001) substrate. The morphology of the deposited GdSt layer and upper Au nanocluster layer were systematically analyzed using atomic force microscopy (AFM) and X-ray reflectivity techniques. The morphology of the Au nanoparticle layer changes remarkably depending on the surface pressure of the Langmuir monolayer employed for its transfer on to the gadolinium stearate layer. Three Langmuir phases at different degrees of compression formed the basis for the chosen surface pressure values for the transfer. The bilayer films are an essentially nanostructured network of islands and interconnects that exhibit nonohmic I–V characteristics when measured laterally across the film using a conducting AFM tip.

Introduction

Electron transport in ultrathin films having a network of metal nanoparticles whose sizes are comparable to the de Broglie wavelength, is an interesting phenomenon.¹ Capped metal nanoclusters possess size-dependent charging energies of the order of hundreds of millielectronvolts and can be used to form these films of metal nanoparticles connected by nonconducting organic molecules, exhibiting nonohmic I–V spectra.² A layer of nanoclusters in these films can be visualized as a network of discrete charging units connected by tunnel junctions, with its characteristics depending both on the nature of the nanoclusters and on the interparticle separation.³ Mott–Hubbard type reversible metal–insulator transitions were observed at room temperature by compressing a Langmuir–Blodgett (LB) film of Ag nanoclusters capped with dodecanethiol.⁴ Tunneling spectroscopic measurements on self-assembled metal nanocluster arrays reveal that at large separation distances, the nanoclusters behave as individual particles, exhibiting a Coulomb staircase and blockade. As the separation distance is lowered, the interparticle interaction energy increases, leading to a finite density of states (DOS) at the Fermi level.⁵ Transport measurements carried out on layer-by-layer assemblies—wherein nanocluster layers interspersed with bifunctional molecules built sequentially⁶ have revealed that transport through such layers can be influenced by altering either the nanocluster diameter or the spacer length.⁷ Similar results have been obtained by studying the conductivity of a two-dimensional array of nanoclusters with patterned electrodes.⁸ In the latter, structural disorder is also known to play a role. By carefully tuning the properties of the nanoclusters and the spacers, nanocrystalline devices capable of lasing and rectification have been obtained.⁹

Systematic studies to understand the relation between morphology and transport property of these films having a mono-

layer of nanocluster is required. In this report, we have presented results of such studies on films of Au nanoclusters grown by LB technique and have demonstrated by atomic force microscopy (AFM) and X-ray reflectivity (XRR) measurements that one can control the morphology of the film simply by choosing an appropriate point on the pressure–area isotherm of the Langmuir monolayer of the nanocluster from which the films are deposited. We have extracted the electron density profile (EDP) as a function of depth and the topography of the surface of the films using XRR and AFM techniques, respectively, to characterize the morphology of the films. We have investigated the transport properties of the deposited Au nanocluster films by employing conducting AFM (C-AFM) and have shown that nonohmic transport properties of these films depend strongly on morphology. The films were obtained by sequential deposition of a monolayer of a fatty acid salt and a layer of Au nanoclusters on a Si(001) surface in a Langmuir–Blodgett (LB) trough. The presence of hydrophobic monolayer of fatty acid salt improves significantly the deposition of Au nanoparticles capped with hydrophobic dodecanethiol. We have used gadolinium stearate (GdSt) as the first deposited layer on Si(001) to form the bilayer film here. It has been shown recently that GdSt exhibit field induced ferromagnetic ordering.¹⁰ This magnetic–nonmagnetic multilayer Au/GdSt/Si system may be an interesting structure to study the spin-dependent transport properties^{11–15} in low dimensions, especially because one can alter the morphology of the film easily by changing deposition pressure.

Experimental Methods

Dodecanethiol encapsulated Au nanoparticles were prepared by the Brust method.¹⁶ The toluene sol containing the dodecanethiol capped nanoparticles was washed thoroughly with water and precipitated with methanol to remove excess reagents. The particles were re-dispersed in toluene for further characterization. Transmission electron microscopic (TEM) measurements were carried out with a JEOL-3010 TEM operating at 300 kV. Samples for TEM were obtained by depositing a drop

* Corresponding author. E-mail: milan@lotus.saha.ernet.in.

[†] Saha Institute of Nuclear Physics.

[‡] Jawaharlal Nehru Center for Advanced Scientific Research.

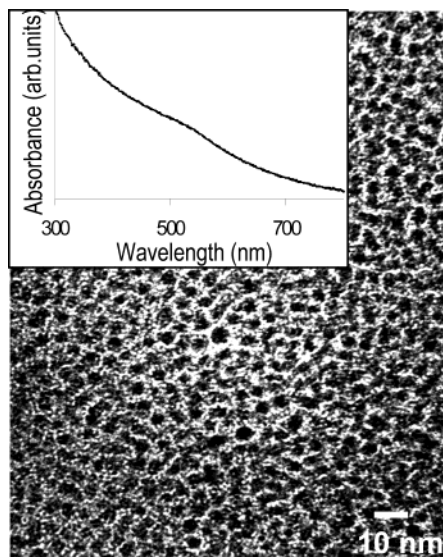


Figure 1. Transmission electron micrograph of Au nanoparticles. The electronic absorption spectra of the Au nanocrystals in toluene, is shown in the inset.

of the toluene sol on a holey carbon copper grid and allowing it to dry in a desiccator overnight. Figure 1 shows a typical TEM micrograph obtained from the Au sol. The mean diameter of the particles was found to be ~ 33 Å. The electronic absorption spectra (Perkin-Elmer Lambda 900) of the Au sol reveals the characteristic plasmon band at 520 nm (see inset of Figure 1). A 1500 μL aliquot of the toluene solution of the Au nanoparticles (0.2 mg/mL) was then spread uniformly on the surface of the Milli-Q water (Millipore) in one of the compartments of an alternating LB trough (KSV 5000). After the solvent evaporated, the hydrophobic dodecanethiol encapsulated Au particles remained on the water surface. The pressure–area isotherm of this Langmuir monolayer was recorded during compression and decompression by moving the barriers at a speed 2 mm/min.

Prior to carrying out sequential deposition, the Si substrate was first made hydrophilic according to the RCA cleaning procedure using ammonia and hydrogen peroxide solutions. In the first step, a layer of GdSt was deposited on it from a monolayer of stearic acid that was spread on the other side of the trough on the water subphase containing 5×10^{-4} M Gd^{3+} ion obtained from dissolved gadolinium acetate.¹⁰ The GdSt monolayer was deposited on the Si substrate by passing it through the monolayer with a water-to-air upstroke at a speed of 3 mm/min. The surface pressure was maintained at a constant value of 30 mN/m during deposition. The dodecanethiol capped Au particles were then transferred to the GdSt/Si substrate during a water-to-air upstroke at a speed of 1 mm/min. Five films (A–E) were deposited at monolayer pressure of 1.5, 2.5, 3.5, 7.0, and 20.0 mN/m, respectively (refer Figure 2c).

The XRR measurements of these films were performed using a 18 kW rotating anode (FR 591Enraf Nonius) X-ray source with $\text{Cu K}\alpha_1$ line monochromatized by a Si(111) crystal.¹⁷ X-ray reflectivity probes the variation in EDP as a function of depth (z) from the surface of a condensed matter system. This technique is of course nondestructive in nature and can be used equally well for studying crystalline and noncrystalline solids and liquid surfaces and interfaces.¹⁷ In X-ray reflectivity measurements, a well collimated monochromatized X-ray beam is made to be incident on the sample surface at grazing angle α (starting from few milliradians) and the reflected intensity is recorded in the plane of incidence at angle β . In specular

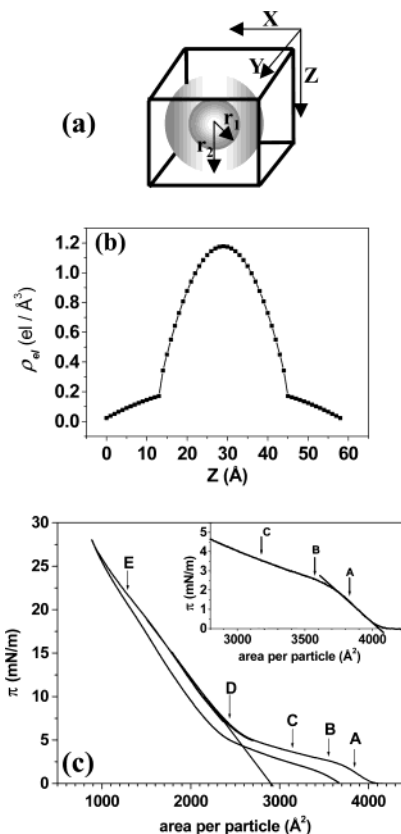


Figure 2. (a) Minimum linear in-plane dimensions (X , Y) of dodecanethiol encapsulated Au nanoparticle are shown schematically. The radii of the Au core and the dodecanethiol capped Au nanoparticle are denoted as r_1 and r_2 , respectively ($2r_1 < 2r_2 = X = Y = Z$). (b) Calculated electron density profile of the dodecanethiol capped Au nanoparticle as a function of depth Z . (c) π – A isotherms obtained while compressing and decompressing a monolayer of Au nanoparticles in a LB trough. Samples A–E were deposited at pressures indicated by the arrows. Phases A–C are shown clearly in the inset by zooming the low-pressure region of the isotherm. The tangents are drawn to indicate the two low compressibility phases.

condition, the incidence angle (α) and scattered angle (β) are equal ($\alpha = \beta = \theta$, for example) and only the nonzero component of the wave vector (\mathbf{q}) is given by $q_z = (4\pi/\lambda) \sin \theta$. Here λ is the wavelength of the X-ray used. For X-rays, the refractive index of any material is slightly less than unity¹⁸ and that gives rise to a positive critical angle, α_c , and corresponding critical wave-vector, q_c . By defining the wave vector as $q_{z,n} = (q_z^2 - q_{c,n}^2)^{1/2}$ in the n th layer of a multilayer structure and roughness σ_n of the interfaces separating two media n and $n + 1$, one can write a recursive relation to calculate reflectivity $R(q_z)$ of the structure.^{17–19} The calculated reflectivity is then fitted to the experimental data to obtain the electron density profile of the multilayer structure.

The AFM measurements of the films were performed using a scanning probe microscope (Nanoscope IV, Digital Instruments) in both tapping and contact modes. The images were obtained using commercially available etched Si (for tapping mode) and Si_3N_4 (for contact mode) cantilevers. The I – V characteristics of the films in ambient conditions were probed using the conducting-AFM set up. This was realized in the contact mode AFM using a conducting cantilever that was prepared by sputter-coating a commercial silicon nitride probe with gold (~ 2 μm thick). A STM stage (Nanoscope II, Digital Instruments) was used to collect the I – V data. The bias voltage was applied to the sample by electrically connecting the STM sample stage to the AFM sample stage. The current was

TABLE 1: Parameters Obtained from AFM and XRR Measurements

	sample A	sample C	sample D	sample E	
				bottom layer	top layer
Parameters Obtained from AFM Measurements					
height of the islands and interconnects as obtained from line profile (Å)	~50	~50	~50	~ 50	~40
coverage of the islands	61%	63%	59%	61%	45%
height variation on islands and interconnects (Å)	±5	±5	±5	±5	±5
saturation value of rms roughness (Å)	24.5	24.1	23.8	25.7	
lateral correlation length (Å)	~6200	~4600	~4000	~3200	
roughness exponent	0.85	0.8	0.72	0.6	
Parameters Obtained from XRR Measurements					
thickness of Au nanoparticle film (Å)	48	48	49	48	42
weighted average electron density of central peak region of EDP (e/Å ³)	0.62	0.62	0.62	0.65	0.47
peak value in EDP (e/Å ³)	0.71	0.73	0.65	0.71	
top surface roughness (Å)	4.0	4.4	4.3	5.0	

measured by the preamp (input resistance 1 MΩ) of Nanoscope II through an electrical connection from the STM tip holder to the cantilever holder. The electrical noise was reduced to less than 0.01 nA by covering the whole setup with a metallic box that was earthed. The I – V plot was acquired by activating the spectroscopy mode of Nanoscope II after falsely engaging it. To ensure that the gold-coating on the cantilever had not worn off while scanning, the cantilever was periodically monitored by collecting I – V data from a reference graphite substrate (HOPG). The top Au films were electrically connected to the steel sample holder by silver paint. After obtaining a good image in the contact mode, the I – V characteristic of the required feature was obtained by positioning the feature to the center of scan area, reducing the scan area to zero, and turning off the feedback. We have obtained two types of I – V curves from each film, one of them with the tip positioned on a cluster top and the other with the tip positioned between two clusters.

Results and Discussion

The pressure–area isotherm obtained during compression and decompression (Figure 2c) show nice reversibility and existence of three different regions. There are two low-compressibility phases at two widely different specific particle areas and there exists a high compressibility phase in between. The low-compressibility low-pressure phase, which extends up to a pressure of 2.0 mN/m (point A, for example), is due to the repulsive interaction arising from the interdigitation of the hydrocarbon tails of dodecanethiol molecules. This steric repulsion is sufficient to counter the van der Waals attraction between the metal cores. This is also the reason the colloidal dispersion of dodecanethiol-capped Au particles remains stable for weeks without aggregation.²⁰ The films deposited beyond a certain surface pressure (~6.0 mN/m indicated by D in Figure 2c) indicate the formation of bilayers of Au clusters themselves, as on the Langmuir monolayer the available volume per cluster reduces drastically and compressibility also decreases. However, it is interesting to note that even beyond this pressure we observed (between points D and E in Figure 2c) the isotherm is retracing the same path during compression and decompression (indicated by the double line). This implies that there is no loss of particles at this pressure range and deformation of the Langmuir monolayer is reversible. But when we decompressed the monolayer from a surface pressure higher than that at point E, the curve does not follow the same path although the nature of the curve is similar throughout. In Figure 2a we have shown minimum linear in-plane dimensions (X , Y) below

which organic tails get compressed into one another, resulting in a reduction in compressibility as observed in phase A of the Langmuir monolayer (refer Figure 2c) at the molecular area ($X \cdot Y$) below 4200 Å². We have also shown the expected electron density profile of a model cluster in Figure 2a, neglecting any surface fluctuations. This model predicts an average electron density of dodecanethiol capped Au cluster as 0.5 $e/\text{Å}^3$ with the Au core contributing 0.83 $e/\text{Å}^3$ having a peak value of 1.18 $e/\text{Å}^3$ (refer Figure 2b). The maximum electron density is found to be quite less here as compared to that of the bulk value of Au (4.4 $e/\text{Å}^3$) because of the presence of organic network. The obtained EDP of the films will be expressed in terms of profiles of Figure 2b centered around different depths to understand the morphology of the deposited films.

We performed systematic AFM studies to extract the real space information regarding height fluctuations and in-plane morphology of the films, and the results are summarized in Table 1. The AFM images of films A–E and that of the GdSt deposited substrate (Figure 3) clearly demonstrate the differences in the surface morphology of the films. The morphology of the GdSt film is quite different, where we observe smooth low roughness (~4 Å) areas consistent with the results obtained in XRR measurements of GdSt film. In all the other films the presence of a network of islands is apparent in the images and the meshes of islands become finer as we go from sample A (Figure 3b) to E (Figure 3e and 3f). We have not shown sample B here, as the morphology of B was similar to that of C. For all the films, the height of the maximum number of islands as well as those of interconnects are about 50 Å, as estimated from the z -profile analysis (shown in Figure 3), and this value matches well with the thickness obtained from X-ray analysis. We notice a height fluctuation of about ±5 Å on the islands and interconnects by drawing a line through them, and this information has been used to extract the EDP of the films from the XRR data. We have also shown a simplified model of the films in Figure 3. The size of the islands and the dimensions of interconnects vary gradually from film A to film E. In sample A, islands are present with a fairly uniform size of 3000 Å and interconnects are ~450 Å thick. Each island has one or two holes marked by arrows in Figure 3b. In sample C (and also in B), the islands are of varied sizes ranging from 600 to 3000 Å. Importantly, the holes in the islands are smaller in diameter but are present with a higher number density (Figure 3c). A very porous structure with 500 Å thick interconnects is observed in sample E with almost no islands and holes (Figure 3e). Moreover, a large number of bright spots corresponding to the

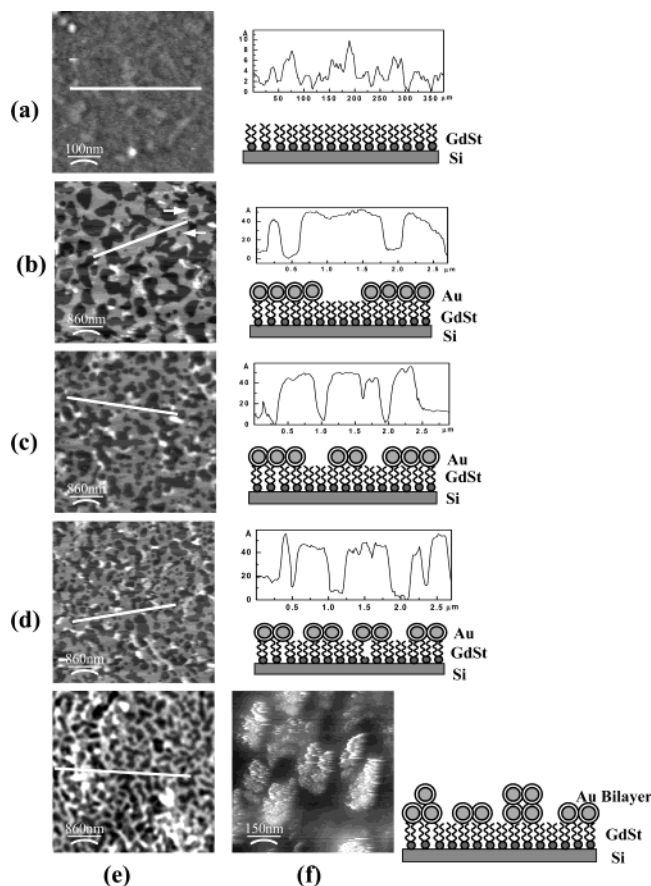


Figure 3. Tapping mode AFM images (from the amplitude channel) of (a) GdSt/Si(001) substrate, (b) sample A, (c) sample C, (d) sample D, (e) sample E, and (f) individual nanoparticles present in the bilayer of sample E. Arrows in (b) indicate the presence of holes in islands. The height profiles corresponding to the lines drawn on respective images are shown for each film and the substrate. The corresponding schematic diagram of the deposited films and the substrate are also shown.

existence of a second Au nanocluster layer, is observed in this case. A high-resolution image of the second layer is shown in Figure 3f, where spherical features with ~ 30 Å height are seen across a background of an inter-linked network.

The monolayer of Au nanoclusters (deposited over GdSt monolayer) goes through substantial restructuring in forming the observed networked membrane. It is interesting to note that despite these variations, the coverage of the islands, estimated on the basis of the area occupied by the island features, is found to be $\sim 60\%$ in all the cases. The growth of the membrane-like structure and its dependence on the surface pressure of the Langmuir monolayer used for deposition, are indeed interesting. Obviously, the surface pressure of the Langmuir monolayer of a Au nanocluster employed in the deposition process and the interaction between the stearic acid chains and dodecanethiol chains both play an important role in determining the variations of network morphology in these films. The nanoparticle film in A was deposited at a lower pressure region of the isotherm where area occupied by each nanoparticle on water surface is high, corresponding to a loosely net monolayer with diminishing interaction among the particles. This monolayer, when transferred to the GdSt, appears to spread like a fluid, tolerating the defects and dislocations of the layer below, thereby forming wide islands with thin interconnects. Because films B–E were obtained at progressively higher compressions, the interparticle separation is greatly reduced, enhancing the interaction among

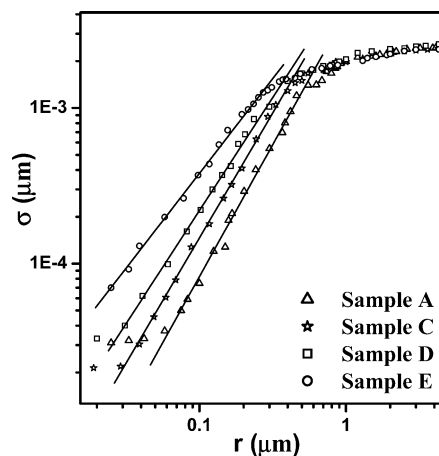


Figure 4. RMS roughness σ vs scan length r obtained from AFM images for four films. The solid lines are fits to the linear portion of the respective curves in log–log scale.

the metal cores. Besides, the neighboring nanoparticles get interlocked due to the increasing interdigitations of the dodecanethiol chains surrounding them. Because of this entanglement of Au nanoclusters the diffusion process^{21,22} after transfer reduces progressively from film B to E and smaller islands with more number of holes are observed.

The lateral correlation present in these films and its dependence on deposition pressure can be extracted from the AFM images. For isotropic self-affine rough surfaces the height–height correlation function $g(r)$, can be written

$$g(r) \equiv \langle [z(0) - z(r)]^2 \rangle = Ar^{2\alpha} \quad (0 < \alpha < 1) \quad (1)$$

where $z(r)$ is the height with respect to a mean surface at a lateral distance r from some origin where the height is $z(0)$, and α is the roughness exponent. The exponent α determines the texture of rough surfaces; a lower α indicates a jagged surface, whereas a higher α implies a surface with relatively smooth fluctuations.²³ All physical systems must exhibit this self-affine scaling only over a finite length scale; otherwise the correlation function defined above would diverge, implying that the roughness would grow indefinitely, which is an unphysical situation. The length scale up to which self-affine scaling is observed in a surface is called the correlation length. For actual physical systems the form of the height height correlation function is modified²³ from that given above to

$$g(r) = 2\sigma^2[1 - \exp(-r/\xi)^{2\alpha}] \quad (2)$$

where σ is the rms roughness of the surface and ξ is the correlation length for self-affine scaling of surface roughness. $g(r)$ has the same form as eq 1 for $r \ll \xi$. It is well-known that, statistically, the scaling of the rms roughness, σ , is equivalent to the scaling of the height–height correlation function, $g(r)$.^{21,24} Figure 4 shows the plot of rms roughness σ against scan length r for scans of different sizes for all the films. The self-affine nature of the films is evident in the log–log plot. In all the films σ increases with r up to a certain cutoff length beyond which it saturates. This cutoff length is the in-plane correlation length ξ , which changes from ~ 6100 Å for film A to ~ 3200 Å for film E. It is interesting to note that in all the films σ saturates to a value ~ 24 Å, which is half the layer thickness. A linear fit to the data shows that the scaling exponent α changes from 0.85 to 0.6 as we go from film A to E. A lower value of α implies more rapid fluctuations in the out of plane direction for sample E due to the presence of the upper cluster layer

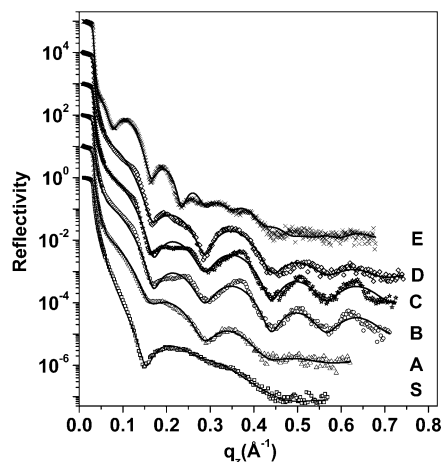


Figure 5. X-ray reflectivity data and fitted curves (solid lines) for five samples (marked A–E) and GdSt/Si(001) substrate (marked as S).

whereas a value of α approaching 1 indicates the presence of relatively smooth islands and valleys in sample A. We have tabulated all these parameters in Table 1. Here we should mention that on the wide islands of film A the rms roughness almost remains unchanged for very small length scales, which is evident from the flat portion of the data for small values of r . We did not observe such a flat portion at low r for other films because the number of smooth wide islands decreases gradually from film A to E. Although a theoretical understanding of the underlying physics giving rise to the membrane-like morphology of the film needs more systematic investigation,^{21,25} it is gratifying that we could control the morphology of these well-defined bilayer films of Au nanoparticle/GdSt on Si(001) substrate.

The XRR data and fitted reflectivity profiles for each of the five films and for the GdSt film are shown in Figure 5. The corresponding electron density profiles were first extracted from the XRR data using a technique based on distorted wave Born approximation.²⁶ In this technique large number of layers of equal thickness (d_i) are used to model EDP of a film, and by fitting the calculated reflectivity with the experimental data, one obtains constant electron densities (ρ_i) for each layer that constitutes the EDP of the film. The consistency of the obtained EDP was verified using the earlier mentioned recursive relation.¹⁸ We have shown in Figure 6 the EDPs obtained from reflectivity profiles and tabulated various parameters in Table 1. The general features of the EDPs match quite well with the schematic model of the deposited films shown in Figure 3. For film A the thickness of the nanoparticle film is obtained as 48 \AA on top of GdSt/Si substrate. The top 14 \AA of the film has an electron density of 0.3 e/\AA^3 , which corresponds to the organic tails (dodecanethiol) surrounding the Au core (refer to Figure 6). Then the electron density increases gradually, attains its highest value (0.71 e/\AA^3) near the center of the film, and again decreases to an intermediate value of 0.48 e/\AA^3 before it reaches the electron density of Gd (0.64 e/\AA^3). The weighted average electron density of the dodecanethiol capped Au nanoparticle layer is found to be $\sim 0.5 \text{ e/\AA}^3$, which matches well with that of the calculated model shown in Figure 2b. The central peak portion in the EDP has a width of about 33 \AA and the weighted average electron density comes out to be 0.62 e/\AA^3 . The contribution of the Au core to the average electron density of a dodecanethiol capped Au nanoparticle layer is less than the obtained calculated value (0.83 e/\AA^3) of the model shown in Figure 2b. The nature of the obtained EDPs for films B–D are

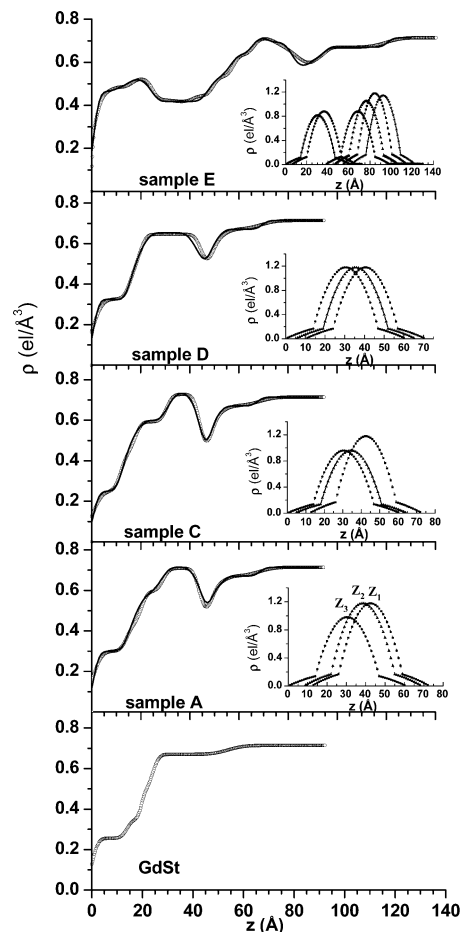


Figure 6. EDPs for samples A, C, D, and E and also for the substrate. The open circles denote the EDPs obtained by fitting XRR data and the solid lines denote the generated profiles calculated using the model. The average vertical positions from bottom (marked as Z_1, Z_2 , etc.) of the Au nanoparticles used for calculation are shown in the insets.

found to be similar to that of film A (refer to Figure 6). In all the cases the thickness of the nanoparticle film is found to be $\sim 48 \text{ \AA}$ and the weighted average electron density of the Au core is $\sim 0.62 \text{ e/\AA}^3$. The average electron density over 48 \AA upper layer comes out to be 0.5 e/\AA^3 in all these films, and these values are consistent with the simple model having average surface area of $\sim 4200 \text{ \AA}^2$ shown in Figure 2a,b. Here we should mention that we are not showing the EDP of film B because the reflectivity profiles and the corresponding EDP of film B and C are almost the same. This is expected as both the films are deposited at a monolayer pressure in the high compressibility phase. For film E, the EDP shows two distinct peaks, each of thickness $\sim 33 \text{ \AA}$, which corresponds to the formation of a bilayer of Au nanoparticles over GdSt layer. The weighted average electron density of the top Au layer is found to be $\sim 0.47 \text{ e/\AA}^3$ whereas that for the bottom one is $\sim 0.65 \text{ e/\AA}^3$, which is higher than the value found in other monolayer films. The lower electron density of the top Au layer indicates that the coverage on the top cluster layer is considerably less. This can be confirmed directly from the AFM image (Figure 3f).

Lowering the electron density of the Au core in all films from the expected peak value of 1.18 e/\AA^3 (as shown in Figure 2b) has occurred because the centers of all the Au clusters in the film are not at the same depth from the top surface. We assume that each film consists of Au clusters having their centers at different depths from the surface with a finite probability of occupation at those depths. To obtain the EDP of this model

TABLE 2: Parameters Used To Calculate the EDP from the Model

	sample A	sample C	sample D	sample E
Z_1-Z_2 (Å)	4	8	5	8.0
Z_2-Z_3 (Å)	8	4	5	8.0
Z_3-Z_4 (Å)				8.0
Z_5-Z_6 (Å)				6.0
A_{12}	1.0	1.23	1.0	0.97
A_{13}	1.2	1.23	1.0	1.09
A_{14}				1.30
A_{15}				1.30
A_{16}				1.41

system, we start with the profile of dodecanethiol capped Au cluster (as shown in Figure 2b) having center at a depth Z_i from the top surface. Let ρ_i be the peak value of electron density at Z_i in this profile. By varying Z and ρ as parameters, one can generate N profiles for clusters having centers at different depths starting from Z_1 to Z_N . The relative probability of occupation at two depths Z_i and Z_j can be determined from the relative amplitude, $A_{ij} = \rho_i/\rho_j$, of the corresponding profiles. The individual profiles can then be added and convoluted with roughness to get the EDP of the film. We tried to keep N a minimum, i.e., used the minimum number of average depths of the nanoclusters in this analysis. We convoluted the profiles with the roughness (σ), which was assumed to have a Gaussian variation of $\sigma \sim 5$ Å, as observed in AFM measurement (Table 1). To simplify the model, we used the same roughness for all clusters. The resultant density profiles match very well with that obtained from XRR measurements even though we have used minimum possible average depths. We used three such average depths, i.e., $N = 3$ for samples A, C, and D. In film E we get a second Au layer and the morphology of the first layer becomes more complicated, as evident from AFM data. We required total of six average depths of Au clusters to describe the obtained EDP of film E properly. The average depths of the Au clusters are marked as Z_1 to Z_6 starting from maximum depth. The parameters used for calculating the EDP from this simple model for all the films are given in Table 2. It is interesting to note that the average depth of Au clusters from the surface increases with deposition pressure as we move from film A to film D. In film D all the three average positions get equally populated.

We have recorded the I – V spectra at different regions on the bilayer samples using a conducting-AFM setup. Here, we report the preliminary results to demonstrate that the transport property of these films depends strongly on morphology. The electrical contacts in these measurements were established directly with the film surface to measure the lateral transport (see schematic in Figure 7a). We plan to study more elaborate electrical transport measurement of these films as a function of temperature and magnetic field. The I – V spectra of Si and GdSt monolayer are shown in Figure 7b. The spectra obtained from sample A and E are shown in Figure 7c,d, respectively. We have obtained two types of I – V curves from each film, one of them with the tip positioned on the cluster top and the other with the tip positioned between clusters. We shall denote the current obtained in these two cases as I_A and I_B , respectively. All the curves are nonlinear in nature. The spectra obtained from the cluster top show a suppression of current near zero bias for ± 150 and ± 500 mV for samples A and E, respectively. The variation of I – V curves obtained from different measurements by positioning the C-AFM tip on different clusters of sample A are indicated by error bars. Here we should mention that the variation in I – V curves obtained from a particular cluster at different times is negligible. In the case of sample A, I_A is quite

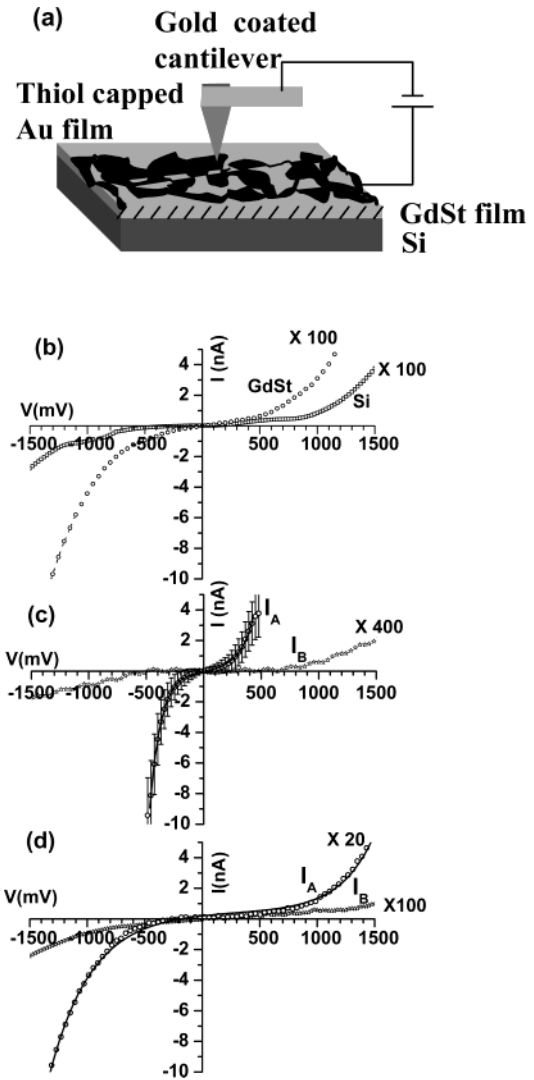


Figure 7. (a) Schematic diagram illustrating the experimental setup. I – V spectra obtained from (b) a bare Si(001) substrate and GdSt/Si layer, (c) film A, and (d) film E. I_A (open circle) and I_B (open star) denote the curves obtained by positioning the tip on cluster top and between clusters. The fitted curves (solid lines) are also shown.

high compared to I_B within the measured voltage range. In sample E, I_A is almost equal to I_B in the lower voltage range. For higher voltages I_A increases more rapidly than I_B . If we compare I_A in two samples we find that the conductivity in sample E is poor, resulting in less current compared to sample A. The curves can be fitted with an exponential decay and growth function of the type

$$I = I_0 + I_1 \exp(-V/V_1) + I_2 \exp(V/V_2) \quad (3)$$

It appears that the nanoparticle film behaves like a network of multiple tunnel junctions where the electrons tunnel through the organic ligands between adjacent metal cores.²⁷ Following an activation, a conduction channel is established through the percolating backbone of nanoparticle interconnects and a stable current is obtained in each case. The current should depend on the interparticle distance, i.e., on the length of the organic linker molecules as well as on the barrier provided by them. Because it is a problem of multiple tunnel junctions, the interparticle distance dependent term in the expression of current will be a summation over the individual tunnel junction.²⁸ If L_{eff} is the effective interparticle distance and β_{eff} is the effective barrier height, then I_1 and I_2 in eq 3 can be written as²⁸ $I_1 = \exp(-\lambda_1)$

and $I_2 = \exp(-\lambda_2)$ with $\lambda = L_{\text{eff}}\beta_{\text{eff}}$. The curves are fitted with eq 3 and the fitted curves are also shown in Figure 7. The value of λ is found to be ~ 2.5 and ~ 6.0 for samples A and E, respectively. Because film E is transferred to the substrate at higher pressure, the organic linker molecules will be compressed in this case, resulting in a smaller interparticle distance in lateral direction. But the higher value of λ for sample E indicates that this film provides a higher barrier to the electrons than in sample A. We have already shown that in sample E the Au particles are not aligned in same plane and the fluctuation in the vertical position of the Au core is more rapid as compared to that in film A, giving rise to a lower scaling exponent α for film E as compared to that of A. This change in morphology in film E may be responsible for the increase in effective barrier for tunneling and hence may reduce the percolation probability for electrons. More detailed study is in progress to explain this morphology dependent electron transport quantitatively.

Summary

We have presented a simple growth technique for preparation of metal–organic bilayer films having magnetic Gd and nonmagnetic Au metallic layers. The morphology of the film could be controlled by choosing appropriate surface pressure for LB deposition. The Langmuir monolayer of Au nanoparticles used for deposition of the film here exhibit three different phases depending on the surface pressure. Corresponding to each phase, a monolayer of Au nanoparticles has been transferred to the GdSt monolayer covered Si(001) substrate to form a nonmagnetic–magnetic bilayer system. Although the thickness and the weighted average electron density of the Au nanoparticle monolayer films do not differ much from one sample to another, the morphology of the film, which has been characterized by AFM and X-ray reflectivity measurements, changes remarkably depending on the Langmuir monolayer phase used for deposition. The films consist of networks of islands that exhibit nonohmic behavior in the current characteristics measured across the film, and the associated barrier heights were found to increase with increasing surface pressure used for deposition.

Acknowledgment. We are grateful to Professor C. N. R. Rao, for useful discussion and encouragement.

References and Notes

- (1) Rao, C. N. R.; Kulkarni, G. U.; Thomas, P. J.; Edwards, P. P. *Chem. Eur. J.* **2002**, 8, 28.
- (2) Thomas, P. J.; Kulkarni, G. U.; Rao, C. N. R. *Chem. Phys. Lett.* **2000**, 321, 163.
- (3) Remacle, F.; Levine, R. D. *ChemPhysChem* **2001**, 2, 20.
- (4) Medeiros-Ribeiro, G.; Ohlberg, D. A. A.; Williams, R. S.; Heath, J. R. *Phys. Rev.* **1999**, B59, 1633.
- (5) Taleb, A.; Silly, F.; Gusev, A. O.; Charra, F.; Pileni, M.-P. *Adv. Mater.* **2000**, 12, 633.
- (6) Bigioni, T. P.; Harrell, L. E.; Cullen, W. G.; Guthrie, D. K.; Whetten, R. L.; First, P. N. *Eur. Phys. J.* **1999**, D6, 355.
- (7) Sarathy, K. V.; Thomas, P. J.; Kulkarni, G. U.; Rao, C. N. R. *J. Phys. Chem.* **1999**, B103, 399.
- (8) Musick, M. D.; Keating, C. D.; Keefe, M. H.; Natan, M. J. *Chem. Mater.* **1997**, 9, 1499.
- (9) Liu, Y.; Wang, Y.; Claus, R. O. *Chem. Phys. Lett.* **1998**, 298, 315.
- (10) Parthasarathy, R.; Lin, X.-M.; Jaeger, H. A. *Phys. Rev. Lett.* **2001**, 87, 186807.
- (11) Schmelzer, J., Jr.; Brown, S. A.; Wurl, A.; Hyslop, M.; Blaikie, R. J. *Phys. Rev. Lett.* **2002**, 88, 226802.
- (12) Doty, R. C.; Yu, H.; Shih, C. K.; Korgel, B. A. *J. Phys. Chem.* **2001**, B105, 8291.
- (13) Sundar, V. C.; Eisler, H.-J.; Bawendi, M. G. *Adv. Mater.* **2002**, 14, 739.
- (14) Cassagneau, T.; Mallouk, T. E.; Fendler, J. H. *J. Am. Chem. Soc.* **1998**, 120, 7848.
- (15) Mukhopadhyay, M. K.; Sanyal, M. K.; Mukadam, M. D.; Yusuf, S. M.; Basu, J. K. *Phys. Rev. B* **2003**, 68, 174427.
- (16) Datta, S.; Das, B. *Appl. Phys. Lett.* **1990**, 56, 665.
- (17) Schmidt, G.; Ferrand, D.; Molenkamp, L. W.; Filip, A. T.; van Wees, B. J. *Phys. Rev.* **2000**, B62, R4790.
- (18) Hanbicki, A. T.; Jonker, B. T.; Itskos, G.; Kioseoglou, G.; Petrou, A. *Appl. Phys. Lett.* **2002**, 80, 1240.
- (19) Barnas, J.; Fert, A. *Phys. Rev. Lett.* **1998**, 80, 1058.
- (20) Yakushiji, K.; Mitani, S.; Takanashi, K.; Takahashi, S.; Maekawa, S.; Imamura, H.; Fujimori, H. *Appl. Phys. Lett.* **2001**, 78, 515.
- (21) Brust, M.; Walker, M.; Bethell, D.; Schiffrin, D. J.; Whyman, R. *Chem. Commun.* **1994**, 801.
- (22) Basu, J. K.; Sanyal, M. K. *Phys. Rep.* **2002**, 363, 1.
- (23) Holy, V.; Pietsch, U.; Baumbach, T. *X-ray Scattering from Thin Films and Multilayers*; Springer: Berlin, 1999.
- (24) Tolan, M. *X-ray Scattering from Soft Matter Thin Films*; Springer: Berlin, 1999.
- (25) Daillant, J.; Gibaud, A. *X-ray and Neutron Reflectivity: Principles and Applications*; Springer: Berlin, 1999.
- (26) Pal, S.; Sanyal, M. K.; Hazra, S.; Kundu, S.; Schreiber, F.; Pflaum, J.; Barrena, E.; Dosch, H. *J. Appl. Phys.* **2004**, 95, 1430.
- (27) Ohara, P. C.; Leff, D. V.; Heath, J. R.; Gelbart, W. M. *Phys. Rev. Lett.* **1995**, 75, 3466.
- (28) Basu, J. K.; Hazra, S.; Sanyal, M. K. *Phys. Rev. Lett.* **1999**, 82, 4675.
- (29) Barabasi, A.-L.; Stanley, H. E. *Fractal Concepts in Surface Growth*; Cambridge University Press: New York, 1995.
- (30) Sinha, S. K.; Sirota, E. B.; Garoff, S.; Stanley, H. B. *Phys. Rev.* **1988**, B38, 2297.
- (31) Basu, J. K.; Sanyal, M. K.; Mukherjee, M.; Banerjee, S. *Phys. Rev.* **2000**, B62, 11109.
- (32) Sharma, A.; Khanna, R. *Phys. Rev. Lett.* **1998**, 81, 3463.
- (33) Sanyal, M. K.; Basu, J. K.; Datta, A.; Banerjee, S. *Europhys. Lett.* **1996**, 36, 265.
- (34) Müller, K.-H.; Herrmann, J.; Raguse, B.; Baxter, G.; Reda, T. *Phys. Rev.* **2002**, B66, 075417.
- (35) Holmlin, R. E.; Haag, R.; Chabynyc, M. L.; Ismagilov, R. F.; Cohen, A. E.; Terfort, A.; Rampi, M. A.; Whitesides, G. M. *J. Am. Chem. Soc.* **2001**, 123, 5075.